

---

# COMPLEX PHYSICS-INFORMED NEURAL NETWORK

---

**Chenhao Si**

School of Data Science  
The Chinese University of Hong Kong, Shenzhen  
Shenzhen, China  
222042011@link.cuhk.edu.cn

**Ming Yan**

School of Data Science  
The Chinese University of Hong Kong, Shenzhen  
Shenzhen, China  
yanming@cuhk.edu.cn

**Xin Li**

Department of Computer Science  
Northwestern University  
IL, USA  
xinli2023@u.northwestern.edu

**Zhihong Xia\***

School of Science, Great Bay University  
Guangdong, China  
& Department of Mathematics  
Northwestern University  
IL, USA  
xia@math.northwestern.edu

February 10, 2025

## ABSTRACT

We propose complex-PINN, a novel physics-informed neural network (PINN) architecture that incorporates a learnable activation function inspired by Cauchy’s integral theorem. By learning the parameters of the activation function, complex-PINN achieves high accuracy with just a single hidden layer. Empirical results show that complex-PINN effectively solves problems where traditional PINNs struggle and consistently delivers significantly higher precision- often by an order of magnitude.

## 1 Introduction

Physics-Informed Neural Networks (PINNs) have emerged as a powerful method for solving both forward and inverse problems involving Partial Differential Equations (PDEs) [1–4]. PINNs leverage the expressive power of neural networks to minimize a loss function that enforces the governing PDEs and boundary/initial conditions. This approach has been widely applied across various domains, including heat transfer [5–7], solid mechanics [8–10], incompressible flows [11–13], stochastic differential equations [14, 15], and uncertainty quantification [16, 17].

Despite their success, PINNs face significant challenges and often struggle to solve certain classes of problems [18, 19]. One major difficulty arises in scenarios where the solution exhibits rapid changes, such as in ‘stiff’ PDEs [20], leading to issues with convergence and accuracy. To address these limitations, researchers have proposed various techniques to improve training efficiency and precision.

Over the years, numerous strategies have been developed to enhance the performance of PINNs, including adaptive weighting of loss functions and selective sampling of training points. For example, Wang et al. [19] leveraged the Neural Tangent Kernel (NTK) to analyze gradient evolution in PINN training, adjusting the weights of each loss component accordingly. Other studies [21, 22] have explored methods for dynamically learning these weights during training. Additionally, adaptive sampling techniques have been introduced to tackle stiff problems by focusing on regions with high residuals. Lu et al. [23] proposed a threshold-based approach for selecting new training points, while Wu et al. [24] introduced a probability density function derived from residuals to improve sampling efficiency. Further extensions include high-dimensional adaptive methods [25] and re-sampling techniques targeting failure regions [26].

Beyond these approaches, causality has been recognized as an influential factor in PINN training [27, 28]. Wang et al. [27] introduced a Causality-PINN, which assigns time-dependent weights to the loss function for time-dependent PDEs, while Daw et al. [28] further integrated causality with importance sampling techniques.

Additional advancements include domain decomposition methods [29–32], improved network initialization schemes [32–34], novel loss functions [35], and alternative network architectures [36–39]. Collectively, these improvements have expanded the capabilities of PINNs for solving complex real-world problems.

However, existing methods primarily rely on additional training techniques or significantly larger models, such as transformers [36] and convolutional neural networks [39]. While these approaches can enhance performance, they also introduce substantial computational overhead. Auxiliary networks and gradient-based modifications [40, 41] increase training costs, whereas larger models suffer from slower convergence due to the large number of parameters [18, 42].

To overcome these limitations, developing a network that enhances both convergence and predictive accuracy without relying on additional training algorithms or significantly increasing model complexity is crucial. Motivated by this, we introduce *compleX*-PINN, which incorporates the Cauchy integral formula [43, 44] into a novel activation function, offering a more efficient and effective alternative to traditional PINNs.

The main contributions of this paper are summarized as follows:

- To the best of our knowledge, this is the first comprehensive study on using Cauchy-based activation functions in PINNs.
- We provide a detailed derivation and motivation for incorporating Cauchy activation functions into PINN architectures.
- Empirical results demonstrate that *compleX*-PINN outperforms several PINN-based models.
- We show that *compleX*-PINN is compatible with existing PINN training techniques, further enhancing its performance when integrated with these methods.

The organization of this paper is as follows. Section 2 provides a brief introduction to PINNs. Our proposed model, *compleX*-PINN, is introduced in Section 3, where we first present the Cauchy activation function using Cauchy’s 1D integral formula in Section 3.1, extend it to high-dimensional cases in Section 3.2, and apply it to neural networks in Section 3.3. Finally, numerical results are presented in Section 4, followed by the conclusion.

## 2 Physics-Informed Neural Network

Denote the spatial domain as  $\Omega \subset \mathbb{R}^n$  with boundary  $\partial\Omega$ , and let  $T$  represent the time domain. The spatial-temporal variable is given by  $(\mathbf{x}, t) \in \Omega \times T$ . A time-dependent partial differential equation (PDE) over this domain is defined as follows:

$$\mathcal{F}[u](\mathbf{x}, t) = 0, \quad (\mathbf{x}, t) \in \Omega \times T, \quad (1)$$

$$\mathcal{B}[u](\mathbf{x}, t) = 0, \quad (\mathbf{x}, t) \in \partial\Omega \times T, \quad (\text{boundary condition}) \quad (2)$$

$$\mathcal{I}[u](\mathbf{x}, 0) = 0, \quad \mathbf{x} \in \Omega, \quad (\text{initial condition}) \quad (3)$$

where  $\mathcal{F}$ ,  $\mathcal{B}$ , and  $\mathcal{I}$  are differential operators, and  $u(\mathbf{x}, t)$  is the solution to the PDE, subject to boundary and initial conditions.

A PINN parameterized by  $\theta$  approximates the solution  $u(\mathbf{x}, t)$ . The input to the neural network is  $(\mathbf{x}, t)$ , and the approximation is denoted by  $\hat{u}(\theta)(\mathbf{x}, t)$ . The PINN minimizes the following objective function:

$$\mathcal{L}(\theta) = \lambda_F \mathcal{L}_F(\theta) + \lambda_B \mathcal{L}_B(\theta) + \lambda_I \mathcal{L}_I(\theta), \quad (4)$$

where

$$\mathcal{L}_F(\theta) = \frac{1}{N_f} \sum_{(\mathbf{x}, t) \in \Omega_F} |\mathcal{F}[\hat{u}(\theta)](\mathbf{x}, t)|^2, \quad (5)$$

$$\mathcal{L}_B(\theta) = \frac{1}{N_b} \sum_{(\mathbf{x}, t) \in \Omega_B} |\mathcal{B}[\hat{u}(\theta)](\mathbf{x}, t)|^2, \quad (6)$$

$$\mathcal{L}_I(\theta) = \frac{1}{N_0} \sum_{(\mathbf{x}, 0) \in \Omega_I} |\mathcal{I}[\hat{u}(\theta)](\mathbf{x}, 0)|^2. \quad (7)$$

Here,  $\Omega_F$ ,  $\Omega_B$ , and  $\Omega_I$  are the training sets for the PDE residual, boundary condition, and initial condition, respectively, with cardinalities  $N_f$ ,  $N_b$ , and  $N_0$ . The weights  $\lambda_F$ ,  $\lambda_B$ , and  $\lambda_I$  are hyper-parameters tuning the contributions of each loss component. Notably,  $\Omega_F$  may include points on the boundary or at the initial time, allowing  $\Omega_F \cap \Omega_B$  and  $\Omega_F \cap \Omega_I$  to be non-empty.

The choice of activation function  $\sigma(\cdot)$  is crucial in PINNs, as it introduces the nonlinearity necessary to approximate complex solutions to PDEs. The hyperbolic tangent (tanh) is commonly used in PINNs for its smoothness and training stability [1, 2]. Wavelet-based activations have also been explored to capture multi-scale features [36, 38, 45]. Recent work by Li et al. [43] proposed the Cauchy activation function, which has shown strong performance in computer vision and time-series forecasting tasks [44].

In this study, we extend the application of the Cauchy activation function to address PDEs that are challenging for standard PINNs. The Cauchy activation function and the novel complex-PINN model are introduced in the following section.

### 3 Complex Physics-Informed Neural Network

The Cauchy activation function, introduced in [43], is defined as:

$$\Phi(x; \mu_1, \mu_2, d) = \frac{\mu_1 x}{x^2 + d^2} + \frac{\mu_2}{x^2 + d^2}, \quad (8)$$

where  $\mu_1$ ,  $\mu_2$ , and  $d$  are trainable parameters. This activation function is inspired by Cauchy's integral formula, as we further elaborate in Section 3.1. We refer to a PINN model employing the Cauchy activation function as complex-PINN.

We would like to note at the outset that our network is initially constructed with a single hidden layer, where each neuron has a unique set of parameters  $\{\mu_1, \mu_2, d\}$ . Consequently, the total number of trainable parameters for the Cauchy activation function is  $3 \times N_{\text{neuron}}$ , where  $N_{\text{neuron}}$  represents the width of the layer.

#### 3.1 1D Cauchy's integral formula and the Cauchy activation function

This section introduces Cauchy's integral formula and derives the Cauchy activation function from it.

**Theorem 1 (Cauchy's Integral Formula)** *Let  $f$  be a complex-valued function on the complex plane. If  $f$  is holomorphic inside and on a simple closed curve  $C$ , and  $z$  is a point inside  $C$ , then:*

$$f(z) = \frac{1}{2\pi i} \oint_C \frac{f(\zeta)}{\zeta - z} d\zeta.$$

Cauchy's integral formula expresses the value of a function at any point  $z$  as a function of known values along a closed curve  $C$  that encloses  $z$ . Remarkably, this principle is akin to machine learning, where the values at new points are inferred from the known values.

In practice, we approximate the integral using a Riemann sum over a finite number of points on the curve  $C$ . Let  $\zeta^1, \zeta^2, \dots, \zeta^m$  be a sequence of  $m$  points on  $C$ . Then,

$$f(z) \approx \frac{1}{2\pi i} \sum_{k=1}^m \frac{f(\zeta^k)}{\zeta^k - z} (\zeta^{k+1} - \zeta^k) := \sum_{k=1}^m \frac{\lambda_k}{\zeta^k - z}, \quad (9)$$

where, for convenience, we set  $\zeta^{m+1} = \zeta^1$  and define  $\lambda_k = \frac{f(\zeta^k)(\zeta^{k+1} - \zeta^k)}{2\pi i}$ .

If our target function  $f$  is real and one-dimensional, we obtain:

$$f(x) \approx \text{Re} \left( \sum_{k=1}^m \frac{\lambda_k}{\zeta^k - x} \right) = \sum_{k=1}^m \frac{\text{Re}(\lambda_k) \text{Re}(\zeta^k) + \text{Im}(\lambda_k) \text{Im}(\zeta^k) - \text{Re}(\lambda_k)x}{(x - \text{Re}(\zeta^k))^2 + (\text{Im}(\zeta^k))^2}. \quad (10)$$

With the Cauchy activation function defined in (8), we have

$$f(x) \approx \sum_{k=1}^m \Phi(x - \text{Re}(\zeta^k); -\text{Re}(\lambda_k), \text{Re}(\lambda_k) \text{Re}(\zeta^k) + \text{Im}(\lambda_k) \text{Im}(\zeta^k), (\text{Im}(\zeta^k))^2). \quad (11)$$

This shows that a one-layer neural network with the Cauchy activation function (8) can approximate the real function  $f(x)$ .

At this point, we would like to highlight the power of the Cauchy approximation. For traditional activation functions such as ReLU or Sigmoid, the best one can hope for is a first-order approximation. However, with the Cauchy approximation, the error term is explicitly produced by approximating the contour integral with discrete values of the function. While we could have used higher-order Newton–Cotes formulas (such as Simpson’s rules or Boole’s rules) for numerical integration, they would yield *exactly the same* Cauchy approximation formula (9). Naturally, the values for  $\lambda_k$  would vary slightly with different integration schemes, but since  $\lambda_k$  are training variables meant to best fit the input data, this variation is inconsequential. Ultimately, the order of approximation can be arbitrarily high. In fact, for any integer  $p$ , the error term is estimated to be of the order  $o(n^{-p})$ .

### 3.2 Multi-dimensional Cauchy’s integral formula

This section extends Cauchy’s integral formula to the multi-dimensional case.

**Theorem 2 (Multi-Dimensional Cauchy’s Integral Formula)** *Let  $f(z)$  be holomorphic in a compact domain  $U \subset \mathbb{C}^N$  within  $N$ -dimensional complex space. For simplicity, assume that  $U$  has a product structure:  $U = U_1 \times U_2 \times \dots \times U_N$ , where each  $U_i$ ,  $i = 1, 2, \dots, N$ , is a compact domain in the complex plane. Let  $P$  denote the surface defined by*

$$P = \partial U_1 \times \partial U_2 \times \dots \times \partial U_N,$$

*then a multi-dimensional extension of Cauchy’s integral formula for  $(z_1, z_2, \dots, z_N) \in U$  is given by:*

$$f(z_1, z_2, \dots, z_N) = \left(\frac{1}{2\pi i}\right)^N \int \dots \int_P \frac{f(\zeta_1, \zeta_2, \dots, \zeta_N)}{(\zeta_1 - z_1)(\zeta_2 - z_2) \dots (\zeta_N - z_N)} d\zeta_1 \dots d\zeta_N.$$

Similarly, we approximate the integral by a Riemann sum over a finite number of points. More precisely, for any integer  $l = 1, \dots, N$ , let  $\zeta_l^1, \zeta_l^2, \dots, \zeta_l^{m_l}$  be a sequence of  $m_l$  points on  $\partial U_l$ . Then,

$$f(z_1, z_2, \dots, z_N) \approx \left(\frac{1}{2\pi i}\right)^N \sum_{k_1=1}^{m_1} \dots \sum_{k_N=1}^{m_N} \frac{f(\zeta_1^{k_1}, \zeta_2^{k_2}, \dots, \zeta_N^{k_N})}{(\zeta_1^{k_1} - z_1)(\zeta_2^{k_2} - z_2) \dots (\zeta_N^{k_N} - z_N)} (\zeta_1^{k_1+1} - \zeta_1^{k_1}) \dots (\zeta_N^{k_N+1} - \zeta_N^{k_N}), \quad (12)$$

where, for convenience, we set  $\zeta_l^{m_l+1} = \zeta_l^1$  for  $l = 1, 2, \dots, N$ .

Collecting all terms that are independent of  $z_1, \dots, z_N$ , we define

$$\lambda_{k_1, \dots, k_N} = \left(\frac{1}{2\pi i}\right)^N f(\zeta_1^{k_1}, \zeta_2^{k_2}, \dots, \zeta_N^{k_N}) (\zeta_1^{k_1+1} - \zeta_1^{k_1}) \dots (\zeta_N^{k_N+1} - \zeta_N^{k_N}),$$

so that we can rewrite the approximation as

$$f(z_1, z_2, \dots, z_N) \approx \sum_{k_1=1}^{m_1} \dots \sum_{k_N=1}^{m_N} \frac{\lambda_{k_1, \dots, k_N}}{(\zeta_1^{k_1} - z_1)(\zeta_2^{k_2} - z_2) \dots (\zeta_N^{k_N} - z_N)}. \quad (13)$$

Since the order of the sample points no longer matters, we can rewrite the sample points as a single sequence  $(\zeta_1^k, \dots, \zeta_N^k)$  for  $k = 1, 2, \dots, m$ , where  $m = m_1 m_2 \dots m_N$ . Thus, we finally obtain

$$f(z_1, z_2, \dots, z_N) \approx \sum_{k=1}^m \frac{\lambda_k}{(\zeta_1^k - z_1)(\zeta_2^k - z_2) \dots (\zeta_N^k - z_N)}, \quad (14)$$

where  $\lambda_1, \lambda_2, \dots, \lambda_m$  are parameters that depend on the sample points  $(\zeta_1^k, \zeta_2^k, \dots, \zeta_N^k)$  and the values  $f(\zeta_1^k, \zeta_2^k, \dots, \zeta_N^k)$  for  $k = 1, 2, \dots, m$ .

### 3.3 Extend the Cauchy activation function to high dimensional space

The Cauchy approximation formula derived above can be computationally inefficient when the dimension  $N$  is high, due to the large number of multiplicative terms in the denominator. Therefore, for large  $N$ , we opt for a simplified representation of the function by applying the Cauchy activation function to linear combinations of the variables. Generally, this corresponds to a dual representation of the function, which is especially efficient for feature-finding in high-dimensional problems. Specifically, we approximate the target function  $f(x_1, x_2, \dots, x_N)$  by

$$f(x_1, x_2, \dots, x_N) \approx \sum_{k=1}^m \Phi(W_{k1}x_1 + W_{k2}x_2 + \dots + W_{kN}x_N + b_k; \mu_{k1}, \mu_{k2}, d_k), \quad (15)$$

where each  $\Phi$  is a Cauchy activation function as defined in Equation (8). Here, the parameters  $W_{k1}, W_{k2}, \dots, W_{kN}$ ,  $b_k, \mu_{k1}, \mu_{k2}$ , and  $d_k$  are trainable, allowing the network to capture the complex relationships among the input variables.

While the theoretical foundation of the approximation involves a single hidden layer, in practice, we can enhance the model's capacity and expressiveness by constructing a neural network with multiple layers. This multilayer approach allows the model to capture hierarchical features and complex dependencies among the input variables, which are especially useful in high-dimensional cases.

Each hidden layer can be viewed as applying a set of nonlinear transformations to the input space, creating intermediate representations that capture interactions across multiple input variables. For a network with  $L$  hidden layers, we recursively define each layer's output as:

$$h^{(l)} = \Phi \left( W^{(l)} h^{(l-1)} + b^{(l)}; \mu^{(l)}, d^{(l)} \right), \quad (16)$$

where  $h^{(l)}$  is the output of the  $l$ -th hidden layer,  $W^{(l)}$  is the weight matrix of layer  $l$ ,  $b^{(l)}$  is the bias vector,  $\mu^{(l)}$  and  $d^{(l)}$  are the parameters of the Cauchy activation function for the  $l$ -th layer.

This recursive formulation allows the network to approximate increasingly complex functions as the number of layers grows, providing both depth and flexibility.

In this way, the network gains both practical advantages from multilayer structures and theoretical grounding from Cauchy's integral approach, providing a novel architecture that can effectively approximate high-dimensional functions.

## 4 Numerical Experiments

In this section, we compare complex-PINN with traditional PINN [1], Residual-Based Attention (RBA) PINN [42], and gradient-enhanced PINN (gPINN) [35] across various partial differential equations (PDEs), including the wave equation (Section 4.1), diffusion-reaction system (Section 4.2), Helmholtz equation (Section 4.3), reaction equation (Section 4.4), and convection equation (Section 4.5).

Complex-PINN is uniquely characterized by a single hidden layer, referred to as the **Cauchy layer**. Unlike other methods, each neuron in the Cauchy layer is parameterized by trainable parameters  $\{\mu_1, \mu_2, d\}$ , which provide greater flexibility in capturing complex solution patterns. Although each neuron introduces three additional parameters, the overall number of trainable parameters in complex-PINN remains significantly smaller than multi-layer architectures used by competing methods, as a single hidden layer is sufficient for high performance. By default, the parameters  $\{\mu_1, \mu_2, d\}$  are initialized to 0.1, unless otherwise specified in particular experiments.

For testing, a uniform grid of points is generated for each dimension. For example, a  $300 \times 300$  grid is used for the 2D case, a  $300 \times 300 \times 300$  grid for the 3D case, and this pattern is extended for higher-dimensional cases. Training points are then randomly sampled from these grids and are kept fixed across methods to ensure consistency. The number of training points is denoted as follows:  $N_f$  for the residual,  $N_b$  for the boundary conditions, and  $N_0$  for the initial conditions.

To guarantee a fair comparison, all experiments are conducted with identical settings, including the learning rate, optimizer, and number of training epochs. Furthermore, the same random seed is used across all methods to enhance reproducibility. However, experimental setups, such as the number of training points or specific network architectures, may vary between PDEs to accommodate their unique characteristics.

Performance is evaluated using the relative  $L^2$  error and the  $L^\infty$  norm, which are defined as follows:

$$\text{(Relative) } L^2 \text{ error} = \frac{\sqrt{\sum_{k=1}^N |\hat{u}(\mathbf{x}_k, t_k) - u(\mathbf{x}_k, t_k)|^2}}{\sqrt{\sum_{k=1}^N |u(\mathbf{x}_k, t_k)|^2}}, \quad (17)$$

$$L^\infty \text{ norm} = \max_{1 \leq k \leq N} |\hat{u}(\mathbf{x}_k, t_k) - u(\mathbf{x}_k, t_k)|, \quad (18)$$

where  $u$  is the true solution of the PDE,  $\hat{u}$  is the output from the tested method, and  $N$  is the number of testing points.

## 4.1 Wave equation

We consider the following 1D wave equation:

$$u_{tt} = 4u_{xx}, \quad x \in [0, 1], t \in [0, 1], \quad (19)$$

$$u(0, x) = \sin(\pi x) + \frac{1}{2} \sin(4\pi x), \quad x \in [0, 1], \quad (20)$$

$$u_t(0, x) = 0, \quad x \in [0, 1], \quad (21)$$

$$u(t, -1) = u(t, 1) = 0, \quad t \in [0, 1], \quad (22)$$

whose exact solution is given by:

$$u(t, x) = \sin(\pi x) \cos(2\pi t) + \frac{1}{2} \sin(4\pi x) \cos(8\pi t). \quad (23)$$

The wave equation is known to be challenging for PINNs due to its stiffness and the resulting difficulty in capturing high-frequency components of the solution [19, 21]. Traditional PINNs have slow convergence and suboptimal predictions. To address this challenge, the Residual-Based Attention (RBA) [42] has been proposed to improve PINNs by dynamically adjusting the weights of training points based on their residuals. RBA adaptively prioritizes regions of the solution domain where the model struggles the most, making it particularly effective for stiff PDEs. The weight  $\lambda_{F_i}$  in Eq. (4) is updated iteratively using the following rule:

$$\lambda_{F_i}^{k+1} = \gamma \lambda_{F_i}^k + \eta \frac{|r_i|}{\|r\|_\infty}, \quad (24)$$

where  $\lambda_{F_i}$  is the weight associated with the training point  $(\mathbf{x}_i, t_i)$ ,  $r_i$  is the residual  $r_i = \mathcal{F}[u](\mathbf{x}_i, t_i)$ , and  $r$  is the residual vector. The hyperparameters  $\gamma$  and  $\eta$  control the contribution of the residual term and its smoothing, and are set as in the original RBA implementation ( $\eta = 0.001$ ,  $\gamma = 0.999$ ). For additional details, refer to [42].

In this experiment, we set  $N_f = 6000$  and the boundary conditions and initial conditions are enforced by the hard constraint formulated as  $\hat{u} = 20x(1-x)t^2 \hat{u}_{NN} + \sin(\pi x) + 0.5 \sin(4\pi x)$  [24, 46, 47], where  $\hat{u}_{NN}$  represents the network output and  $\hat{u}$  denotes the final prediction. For the standard PINN and RBA, we use a network with 5 hidden layers, each containing 300 neurons. For the compleX-PINN, we adopt a single hidden layer architecture with 1000 neurons. The number of parameters for PINN and RBA are  $3 \times 300 + 301 \times 300 \times 4 + 301 \times 1 = 362,401$ , while that for compleX-PINN is only  $6 \times 1000 + 1001 \times 1 = 7,001$ . Both models are trained using the Adam optimizer with a learning rate of  $4 \times 10^{-5}$  for 100k iterations.

The results of these experiments are presented in Fig. 1 and Fig. 2, with numerical results summarized in Table 1. As illustrated in Fig. 2, the standard PINN consistently exhibits a high relative  $L^2$  error (more than 0.4) throughout training, highlighting its difficulty in solving stiff PDEs, as also reported in [19, 21]. When the Residual-Based Attention (RBA) technique is applied to the standard PINN, the relative  $L^2$  error decreases rapidly, reaching 0.02 at 20k iterations and increasing to 0.08 at 100k iterations, showcasing the effectiveness of RBA in addressing these challenges.

In comparison, compleX-PINN alone achieves significantly more accurate predictions, reducing the relative  $L^2$  error rapidly to below 0.01 within just 20k iterations. When further enhanced with RBA (referred to as compleX-RBA), the relative  $L^2$  error reduces from  $3.01 \times 10^{-3}$  to  $1.14 \times 10^{-3}$  after 100k iterations, demonstrating the synergistic effectiveness of combining compleX-PINN with RBA for solving stiff wave equations.

Table 1: Final performance of different models for the 1D wave equation after 100k iterations.

Model	Relative $L^2$ error	$L^\infty$ norm
PINN [1]	$6.26 \times 10^{-1}$	$7.56 \times 10^{-1}$
RBA [42]	$8.57 \times 10^{-2}$	$2.30 \times 10^{-1}$
compleX-PINN	$3.01 \times 10^{-3}$	$6.33 \times 10^{-3}$
compleX-RBA	<b><math>1.14 \times 10^{-3}</math></b>	<b><math>2.03 \times 10^{-3}</math></b>

## 4.2 Diffusion-reaction Equation

The diffusion-reaction equation, a parabolic PDE, models the macroscopic behavior of particles undergoing Brownian motion combined with chemical reactions. It finds applications in various fields, including information theory, materials

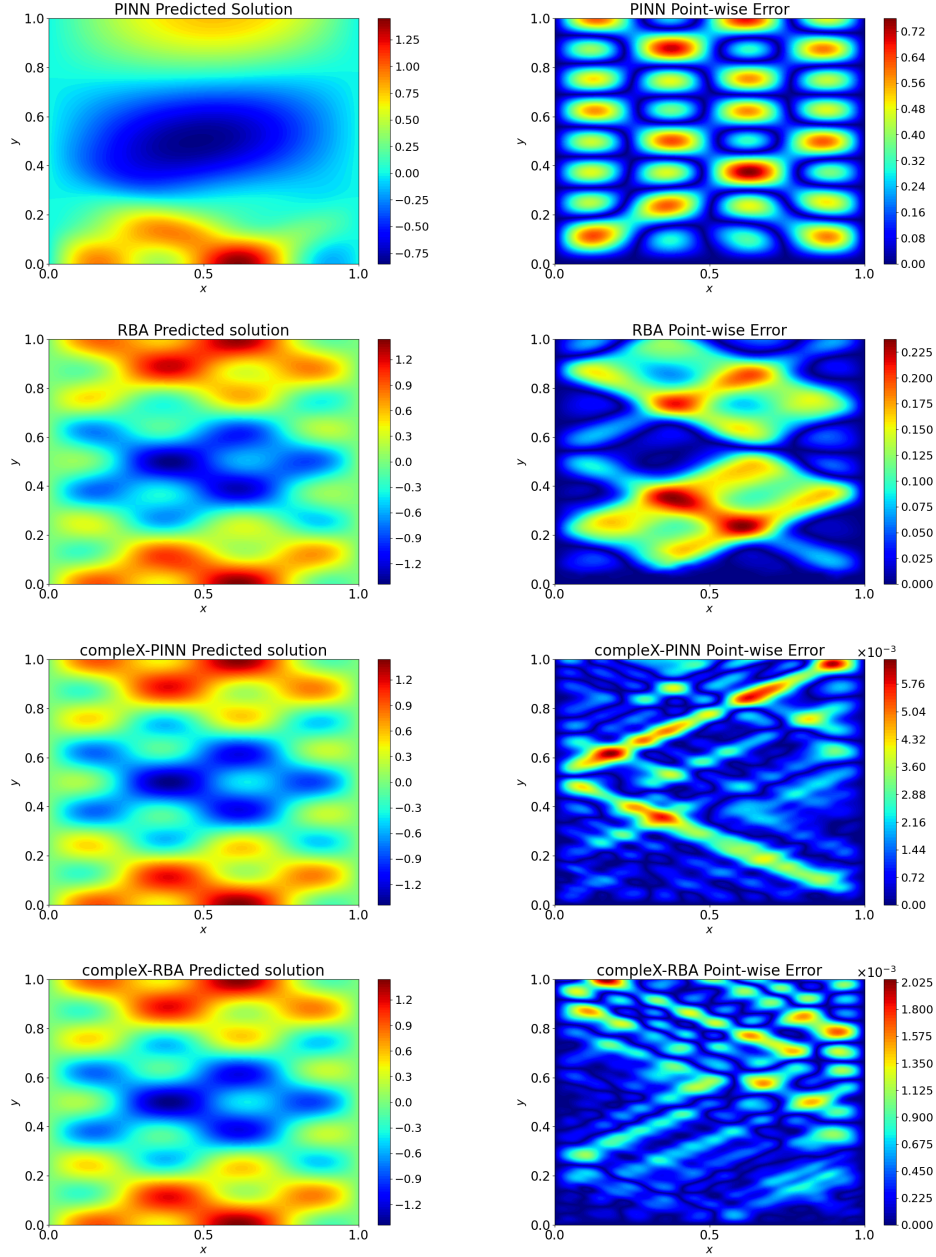


Figure 1: Prediction and pointwise error for the 1D wave equation using four methods: standard PINN (first row), RBA-PINN (second row), complexX-PINN (third row), and complexX-RBA (last row). ComplexX-PINN achieves an  $L^\infty$  error of  $6.33 \times 10^{-3}$ , which is further reduced to  $2.03 \times 10^{-3}$  when the RBA technique is applied to complexX-PINN.

science, and biophysics. In this section, we consider the following system, identical to the one presented in Ref. [35]:

$$u_t = u_{xx} + R(x, t), \quad x \in [-\pi, \pi], t \in [0, 1], \quad (25)$$

$$u(\pi, t) = u(-\pi, t) = 0, \quad (26)$$

$$u(x, 0) = \sum_{n=1}^4 \frac{\sin(nx)}{n} + \frac{\sin(8x)}{8}, \quad (27)$$

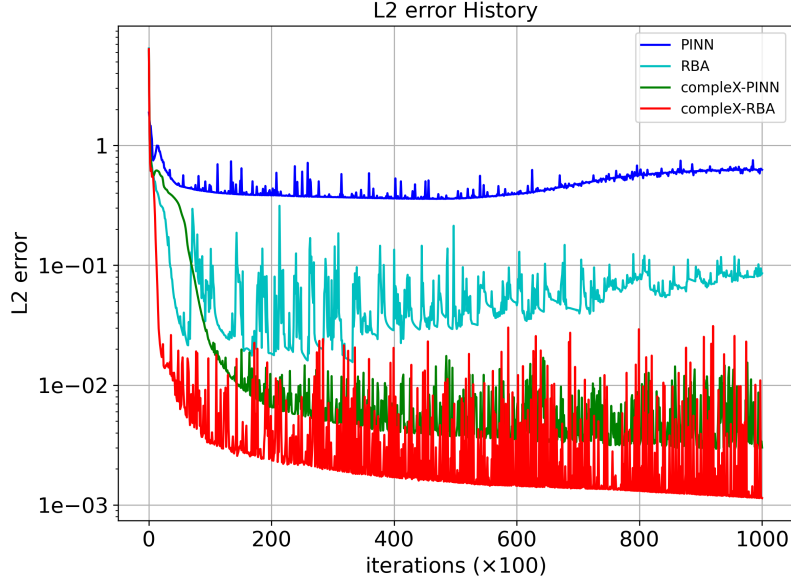


Figure 2: Relative  $L^2$  error history of PINN, RBA, complexX-PINN, and complexX-RBA for the 1D Wave equation. complexX-PINN outperforms both the standard PINN and RBA, and its performance is further improved when combined with the RBA technique.

where  $R(x, t)$  represents the reaction term:

$$R(x, t) = e^{-t} \left[ \frac{3}{2} \sin(2x) + \frac{8}{3} \sin(3x) + \frac{15}{4} \sin(4x) + \frac{63}{8} \sin(8x) \right]. \quad (28)$$

The analytical solution to this system is given by:

$$u(x, t) = e^{-t} \left( \sum_{n=1}^4 \frac{\sin(nx)}{n} + \frac{\sin(8x)}{8} \right). \quad (29)$$

For this experiment, we set  $N_f = 500$  and  $N_0 = N_b = 50$ . We compare complexX-PINN with RBA and Gradient-Enhanced PINN (gPINN) [35]. The complexX-PINN uses a hidden layer with 1500 neurons, while RBA and gPINN employ a 4-layer neural network with 100 neurons per hidden layer. All models are trained using the Adam optimizer with a learning rate of  $1 \times 10^{-5}$  for 15k iterations.

The predictions and pointwise errors are illustrated in Fig. 3, while the relative  $L^2$  error histories are shown in Fig. 4. The results demonstrate that complexX-PINN converges much faster to a lower relative  $L^2$  error compared to the other methods.

### 4.3 2D Helmholtz equation

The Helmholtz equation describes wave and diffusion phenomena, addressing variations over time within a spatial or combined spatial-temporal domain. We consider the following 2D Helmholtz equation

$$u_{xx} + u_{yy} + k^2 u - q(x, y) = 0, \quad (x, y) \in \Omega, \quad (30)$$

$$u(x, y) = 0, \quad (x, y) \in \partial\Omega, \quad (31)$$

where

$$q(x, y) = (k^2 - 2(a\pi)^2) \sin(a\pi x) \sin(a\pi y). \quad (32)$$

We set  $k = 1$  and  $\Omega = [-1, 1] \times [-1, 1]$  and the exact solution to the equation is

$$u(x, y) = \sin(a\pi x) \sin(a\pi y). \quad (33)$$



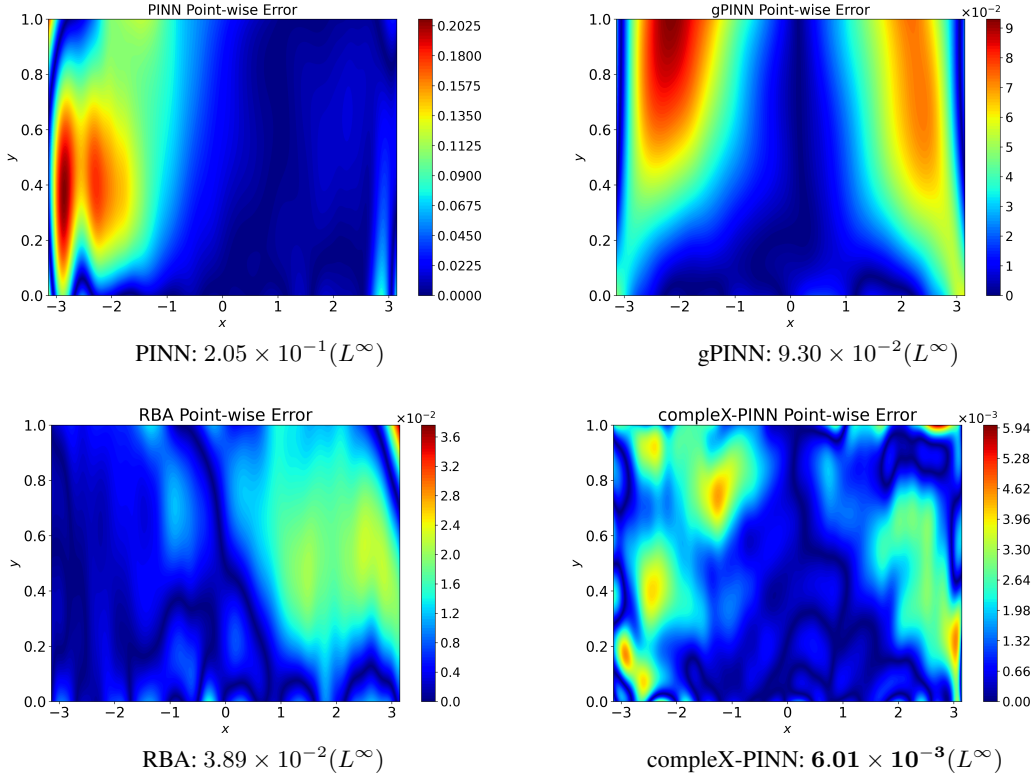


Figure 3: Pointwise error for the diffusion-reaction system using four methods: PINN, gPINN, RBA, and compleX-PINN. Among them, compleX-PINN exhibits the smallest  $L^\infty$  error, while the errors of the other methods are more than six times larger.

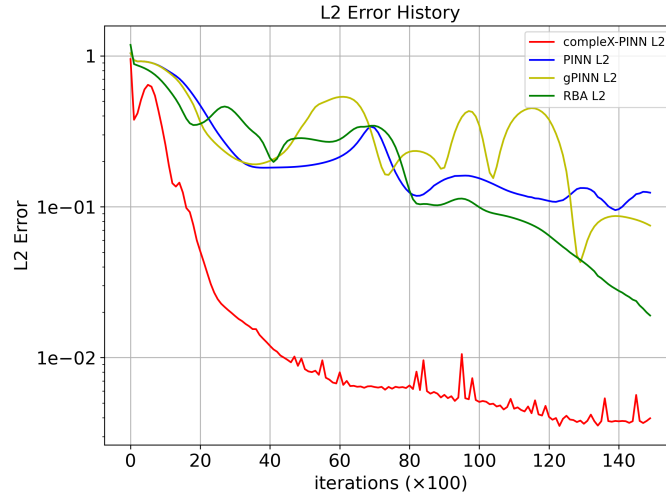


Figure 4: Relative  $L^2$  error history of different models for the diffusion-reaction equation. CompleX-PINN achieves a significantly lower relative  $L^2$  error compared to all other models, and does so in fewer iterations. Specifically, compleX-PINN reduces the error below  $1 \times 10^{-2}$  within 5k iterations, whereas other models reach their lowest error of approximately  $2 \times 10^{-2}$  only after 15k iterations.

In this study, we focus on two different settings for parameter  $a \in \{3, 6\}$  in the forcing term  $q(x, y)$ , where the corresponding exact solution can be viewed in Fig. 5. For both cases, we compare the compleX-PINN with the traditional PINN and RBA.

All PINN-based models employ a 5-layer network architecture, each layer consisting of 60 neurons. The complexX-PINN uses a Cauchy layer with 1000 neurons. Training is conducted using the Adam optimizer for 10k iterations with a learning rate of  $1 \times 10^{-4}$ . Furthermore, we set  $N_f = 5000$  for each model. Boundary conditions are implemented using a hard constraint formulated as  $\hat{u} = (x^2 - 1)(y^2 - 1)\hat{u}_{NN}$  [42, 46, 47]. As a result, only the residual loss (5) is enforced, and no boundary training points are included.

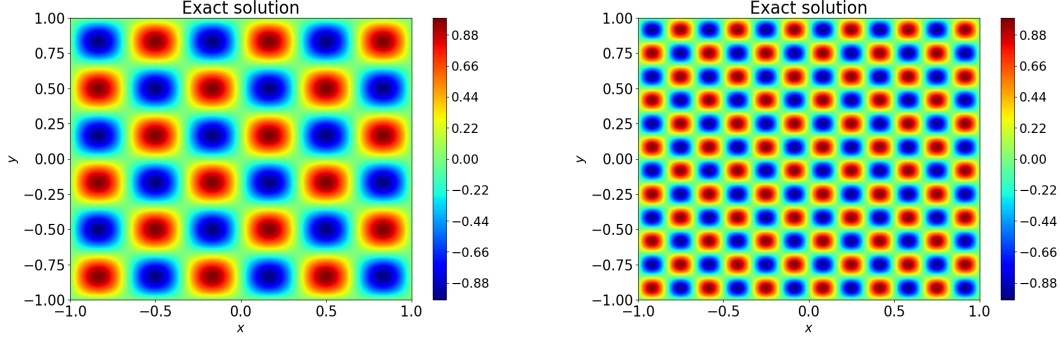


Figure 5: The exact solutions for the 2D Helmholtz equation when  $a = 3$  (left) and  $a = 6$  (right).

The results for each model can be visualized in Fig. 6. For  $a = 3$ , both PINN and RBA exhibit significant errors spread across the domain, while complexX-PINN accurately predicts the solution across nearly the entire domain, with only small localized errors. Moreover, the maximum error for complexX-PINN ( $2.11 \times 10^{-3}$ ) is substantially lower than those of PINN ( $9.02 \times 10^{-2}$ ) and RBA ( $3.01 \times 10^{-2}$ ).

Moreover, for the  $a = 6$  case, point-wise error comparisons across PINN, RBA, and complexX-PINN highlight the better accuracy of complexX-PINN. The PINN prediction exhibits regions of significant error, particularly near the boundaries and in specific interior areas, with a maximum error of 0.383. The RBA method reduces these errors but still shows localized high-error regions, achieving a maximum error of 0.146. In contrast, complexX-PINN demonstrates substantially improved performance with a significantly lower maximum error of  $1.97 \times 10^{-2}$ .

The relative  $L^2$  error history is shown in Fig. 7. We can see the relative  $L^2$  errors for complexX-PINN decrease faster to lower values, compared with PINN and RBA. These results underscore the effectiveness of complexX-PINN in achieving higher accuracy and better error control compared to the baseline methods.

#### 4.4 Reaction equation

The reaction problem is a hyperbolic PDE used to model chemical reactions, formulated with periodic boundary conditions as follows:

$$u_t - \rho u(1 - u) = 0, \quad x \in [0, 2\pi], \quad t \in [0, 1], \quad (34)$$

$$u(0, t) = u(2\pi, t), \quad t \in [0, 1], \quad (35)$$

$$u(x, 0) = u_0(x), \quad x \in [0, 2\pi]. \quad (36)$$

The system has an analytical solution in the form:

$$u(x, t) = \frac{u_0(x)e^{\rho t}}{u_0(x)e^{\rho t} + 1 - u_0(x)}. \quad (37)$$

We define the initial condition as:

$$u_0(x) = \exp\left(-\frac{(x - \pi)^2}{2(\pi/4)^2}\right). \quad (38)$$

We evaluate the performance of PINN, RBA, complexX-PINN, and complexX-RBA for  $\rho \in \{5, 10, 15, 20\}$ . We set  $N_f = 6000$  and  $N_0 = N_b = 150$ . PINN is set to be a 5-layer network with 80 neurons in each hidden layer and complexX-PINN has 1200 neurons for the Cauchy layer. Training is conducted using the Adam optimizer with a learning rate of  $5 \times 10^{-4}$  for 10k iterations. The relative  $L^2$  error for all models are shown in Fig. 8 and Table 2. This figure illustrates that solving the PDE becomes increasingly challenging as the parameter  $\rho$  grows larger. Notably,

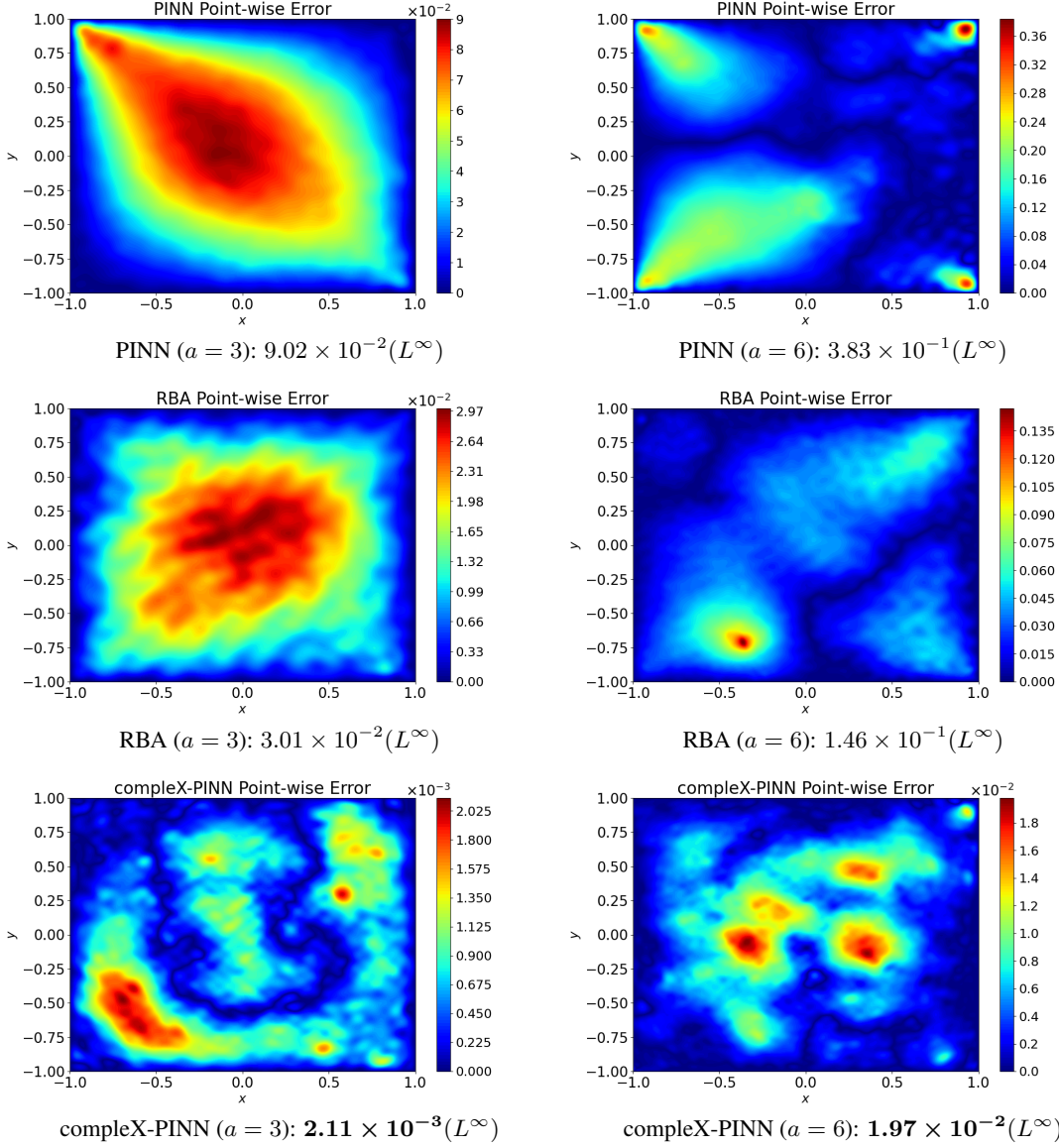


Figure 6: Point-wise errors for traditional PINN (first row), RBA (second row), and complex-PINN (third row), respectively. The first column stands for the results for  $a = 3$  and the second is for  $a = 6$ . complex-PINN receives a lower  $L^\infty$  error for both cases, compared with PINN and RBA.

complex-PINN consistently outperforms PINN and RBA, demonstrating its ability to handle higher stiffness in the reaction equation. Besides, complex-RBA can reduce the relative  $L^2$  errors to a lower value. This further demonstrates the potential of our model, suggesting that its performance can be enhanced by incorporating techniques originally proposed for PINNs, consistent with the conclusion in Section 4.1.

Table 2: Relative  $L^2$  errors of the reaction equation for different models with  $\rho \in \{5, 10, 15, 20\}$  after 10k iterations.

$\rho$ value	PINN	RBA	complex-PINN	complex-RBA
5	$6.90 \times 10^{-2}$	$3.31 \times 10^{-2}$	$7.04 \times 10^{-3}$	<b><math>4.23 \times 10^{-3}</math></b>
10	$9.64 \times 10^{-1}$	$3.40 \times 10^{-2}$	$1.38 \times 10^{-2}$	<b><math>4.75 \times 10^{-3}</math></b>
15	$9.65 \times 10^{-1}$	$4.15 \times 10^{-2}$	$1.52 \times 10^{-2}$	<b><math>5.07 \times 10^{-3}</math></b>
20	$9.91 \times 10^{-1}$	$6.42 \times 10^{-2}$	$1.18 \times 10^{-2}$	<b><math>6.23 \times 10^{-3}</math></b>

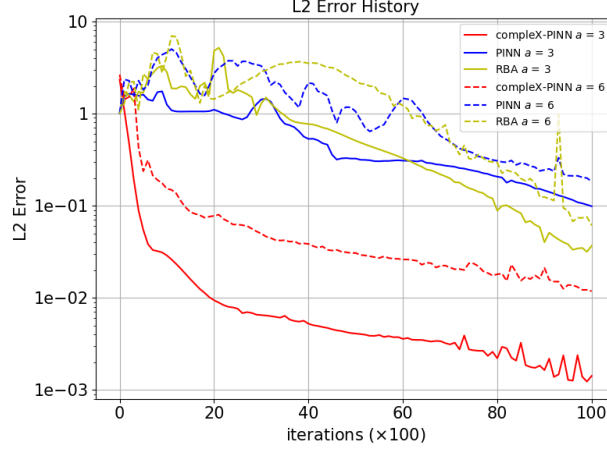


Figure 7: Relative  $L^2$  error history of PINN, RBA, and complexX-PINN for the 2D Helmholtz equation for  $a = 3$  and 6. ComplexX-PINN converges faster to a lower value. E.g., when  $a = 3$ , the  $L^2$  error is reduced to below 0.01 for about 20k iterations, while the errors for the other two models can only archive the lowest value around 0.03.

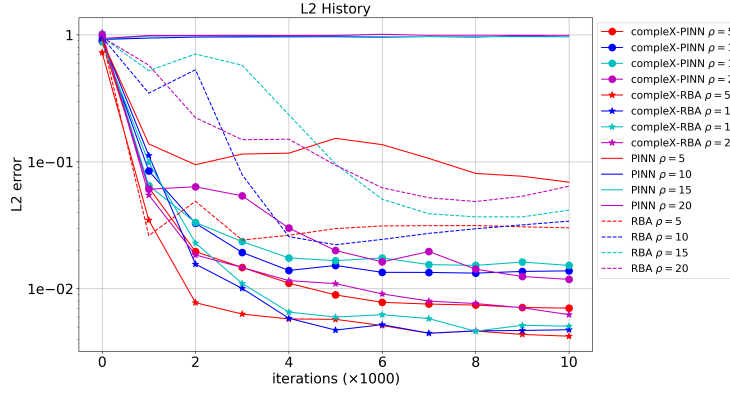


Figure 8: Relative  $L^2$  error history of PINN, RBA, complexX-PINN, and complexX-RBA for the reaction equation with  $\rho \in \{5, 10, 15, 20\}$ . In detail, PINN fails to train for large  $\rho \in \{10, 15, 20\}$ . Although RBA can make the relative  $L^2$  errors to be below  $1 \times 10^{-1}$ , complexX-PINN consistently outperforms them. The highest relative  $L^2$  of complexX-PINN at 10k iteration for different  $\rho$  values is about  $1.52 \times 10^{-2}$  and the lowest can achieve  $7.04 \times 10^{-3}$ . Also, when we use the RBA technique to complexX-PINN, complexX-RBA can reduce the errors to lower values.

#### 4.5 Convection equation

The convection equation [28, 36, 48, 49] describes the transport of a conserved scalar field by a velocity field over time. This equation is widely applied in fluid dynamics and other related fields. We consider the following equation:

$$u_t + \beta u_x = 0, \quad (x, t) \in [0, 2\pi] \times [0, 1], \quad (39)$$

$$u(0, t) = u(2\pi, t), \quad t \in [0, 1], \quad (40)$$

$$u(x, 0) = \sin(x), \quad x \in [0, 2\pi], \quad (41)$$

with the corresponding exact solution:

$$u(x, t) = \sin(x - \beta t), \quad (42)$$

which oscillates periodically between  $-1$  and  $1$  and  $\beta$  denotes the constant velocity parameter.

Previous studies have successfully trained PINNs for  $\beta = 50$ , including approaches such as importance sampling [28], transformer-based PINN [36], and sequence-to-sequence learning [48]. A more recent work [49] extended this to

$\beta = 100$ , which improves the accuracy of PINNs for time-dependent problems by exactly enforcing temporal continuity between sequential time segments through a solution ansatz. The lowest relative  $L^2$  error recorded in Ref. [49] for  $\beta = 50$  and 100 is  $3.75 \times 10^{-3}$  and  $6.28 \times 10^{-3}$ , respectively.

However, as  $\beta$  increases further, the complexity of the problem increases significantly, making it increasingly difficult for traditional PINNs to maintain accurate predictions. The aforementioned works do not extend to higher  $\beta > 100$ . To address this, we extend the research by testing complex-PINN for higher values of  $\beta$ , specifically for  $\beta \in \{50, 80, 90, 100, 120, 150\}$ .

We use 2500 neurons for the Cauchy layer and set  $N_f = 50 \times \beta$  and  $N_0 = N_b = 100$ . The complex-PINN is trained using the Adam optimizer with a learning rate of  $5 \times 10^{-4}$  over 100k iterations.

The relative  $L^2$  error history is shown in Fig. 9, and the final performance after training is summarized in Table 3. The performance for  $\beta = 50$  and  $\beta = 100$  exceeds that reported in Ref. [49]. Furthermore, we extend the analysis to  $\beta = 120$  and  $\beta = 150$ , both of which achieve relative  $L^2$  errors below  $1 \times 10^{-2}$ .

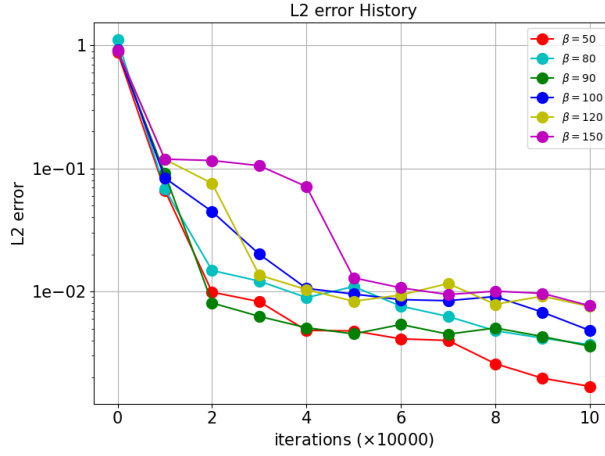


Figure 9: Relative  $L^2$  error history of complex-PINN for the convection equation with  $\beta \in \{50, 80, 90, 100, 120, 150\}$ .

Table 3: Final relative  $L^2$  error of complex-PINN for the convection equation after 100k iterations with different  $\beta$ .

	$\beta = 50$	$\beta = 80$	$\beta = 90$	$\beta = 100$	$\beta = 120$	$\beta = 150$
Relative $L^2$ error	$1.69 \times 10^{-3}$	$3.69 \times 10^{-3}$	$3.59 \times 10^{-3}$	$4.82 \times 10^{-3}$	$7.54 \times 10^{-3}$	$7.66 \times 10^{-3}$

## 5 Conclusion

In this paper, we introduce complex-PINN, which is a single-layer network that utilizes the Cauchy integral formula. Complementing our theoretical advances, the empirical results show that complex-PINN can achieve a much lower relative  $L^2$  error with fewer iterations. Also, the number of parameters in complex-PINN is much smaller than in the traditional PINN. This enhanced efficiency and accuracy validate the efficacy of our theoretical contributions and highlight the practical advantages of complex-PINN.

## Acknowledgments

This work was partially supported by the National Natural Science Foundation of China (72495131, 82441027), Guangdong Provincial Key Laboratory of Mathematical Foundations for Artificial Intelligence (2023B1212010001), Shenzhen Stability Science Program, and the Shenzhen Science and Technology Program under grant no. ZDSYS20211021111415025.

## References

- [1] M. Raissi, P. Perdikaris, and G. E. Karniadakis. Physics-informed neural networks: A deep learning framework for solving forward and inverse problems involving nonlinear partial differential equations. *Journal of Computational Physics*, 378:686–707, 2019.
- [2] George Em Karniadakis, Ioannis G Kevrekidis, Lu Lu, Paris Perdikaris, Sifan Wang, and Liu Yang. Physics-informed machine learning. *Nature Reviews Physics*, 3(6):422–440, 2021.
- [3] Yuyao Chen, Lu Lu, George Em Karniadakis, and Luca Dal Negro. Physics-informed neural networks for inverse problems in nano-optics and metamaterials. *Optics express*, 28(8):11618–11633, 2020.
- [4] Minglang Yin, Xiaoning Zheng, Jay D Humphrey, and George Em Karniadakis. Non-invasive inference of thrombus material properties with physics-informed neural networks. *Computer Methods in Applied Mechanics and Engineering*, 375:113603, 2021.
- [5] Shengze Cai, Zhicheng Wang, Sifan Wang, Paris Perdikaris, and George Em Karniadakis. Physics-informed neural networks for heat transfer problems. *Journal of Heat Transfer*, 143(6):060801, 2021.
- [6] Shengze Cai, Zhicheng Wang, Chrysostomos Chrysostomidis, and George Em Karniadakis. Heat transfer prediction with unknown thermal boundary conditions using physics-informed neural networks. In *Fluids Engineering Division Summer Meeting*, volume 83730, page V003T05A054. American Society of Mechanical Engineers, 2020.
- [7] Jiang-Zhou Peng, Yue Hua, Yu-Bai Li, Zhi-Hua Chen, Wei-Tao Wu, and Nadine Aubry. Physics-informed graph convolutional neural network for modeling fluid flow and heat convection. *Physics of Fluids*, 35(8), 2023.
- [8] Jinshuai Bai, Timon Rabczuk, Ashish Gupta, Laith Alzubaidi, and Yuantong Gu. A physics-informed neural network technique based on a modified loss function for computational 2d and 3d solid mechanics. *Computational Mechanics*, 71(3):543–562, 2023.
- [9] Ehsan Haghghat, Maziar Raissi, Adrian Moure, Hector Gomez, and Ruben Juanes. A physics-informed deep learning framework for inversion and surrogate modeling in solid mechanics. *Computer Methods in Applied Mechanics and Engineering*, 379:113741, 2021.
- [10] Enrui Zhang, Ming Dao, George Em Karniadakis, and Subra Suresh. Analyses of internal structures and defects in materials using physics-informed neural networks. *Science advances*, 8(7):eabk0644, 2022.
- [11] Shengze Cai, Zhiping Mao, Zhicheng Wang, Minglang Yin, and George Em Karniadakis. Physics-informed neural networks (pinns) for fluid mechanics: A review. *Acta Mechanica Sinica*, 37(12):1727–1738, 2021.
- [12] Xiaowei Jin, Shengze Cai, Hui Li, and George Em Karniadakis. Nsfnets (navier-stokes flow nets): Physics-informed neural networks for the incompressible navier-stokes equations. *Journal of Computational Physics*, 426:109951, 2021.
- [13] Ameya D Jagtap, Zhiping Mao, Nikolaus Adams, and George Em Karniadakis. Physics-informed neural networks for inverse problems in supersonic flows. *Journal of Computational Physics*, 466:111402, 2022.
- [14] Jared O’Leary, Joel A Paulson, and Ali Mesbah. Stochastic physics-informed neural ordinary differential equations. *Journal of Computational Physics*, 468:111466, 2022.
- [15] Liu Yang, Dongkun Zhang, and George Em Karniadakis. Physics-informed generative adversarial networks for stochastic differential equations. *SIAM Journal on Scientific Computing*, 42(1):A292–A317, 2020.
- [16] Yibo Yang and Paris Perdikaris. Adversarial uncertainty quantification in physics-informed neural networks. *Journal of Computational Physics*, 394:136–152, 2019.
- [17] Liu Yang, Xuhui Meng, and George Em Karniadakis. B-pinns: Bayesian physics-informed neural networks for forward and inverse pde problems with noisy data. *Journal of Computational Physics*, 425:109913, 2021.
- [18] Sifan Wang, Yujun Teng, and Paris Perdikaris. Understanding and mitigating gradient flow pathologies in physics-informed neural networks. *SIAM Journal on Scientific Computing*, 43(5):A3055–A3081, 2021.
- [19] Sifan Wang, Xinling Yu, and Paris Perdikaris. When and why pinns fail to train: A neural tangent kernel perspective. *Journal of Computational Physics*, 449:110768, 2022.
- [20] RL Burden, JD Faires, and AM Burden. Numerical analysis (10th). *Cengage Learning*, 2015.
- [21] Levi D McClenny and Ulisses M Braga-Neto. Self-adaptive physics-informed neural networks. *Journal of Computational Physics*, 474:111722, 2023.
- [22] Yanjie Song, He Wang, He Yang, Maria Luisa Taccari, and Xiaohui Chen. Loss-attentional physics-informed neural networks. *Journal of Computational Physics*, 501:112781, 2024.

- [23] Lu Lu, Xuhui Meng, Zhiping Mao, and George Em Karniadakis. Deepxde: A deep learning library for solving differential equations. *SIAM review*, 63(1):208–228, 2021.
- [24] Chenxi Wu, Min Zhu, Qinyang Tan, Yadhu Kartha, and Lu Lu. A comprehensive study of non-adaptive and residual-based adaptive sampling for physics-informed neural networks. *Computer Methods in Applied Mechanics and Engineering*, 403:115671, 2023.
- [25] Shaojie Zeng, Zong Zhang, and Qingsong Zou. Adaptive deep neural networks methods for high-dimensional partial differential equations. *Journal of Computational Physics*, 463:111232, 2022.
- [26] Zhiwei Gao, Liang Yan, and Tao Zhou. Failure-informed adaptive sampling for pinns. *SIAM Journal on Scientific Computing*, 45(4):A1971–A1994, 2023.
- [27] Sifan Wang, Shyam Sankaran, and Paris Perdikaris. Respecting causality for training physics-informed neural networks. *Computer Methods in Applied Mechanics and Engineering*, 421:116813, 2024.
- [28] Arka Daw, Jie Bu, Sifan Wang, Paris Perdikaris, and Anuj Karpatne. Rethinking the importance of sampling in physics-informed neural networks. *arXiv preprint arXiv:2207.02338*, 2022.
- [29] Ameya D Jagtap and George Em Karniadakis. Extended physics-informed neural networks (xpinns): A generalized space-time domain decomposition based deep learning framework for nonlinear partial differential equations. *Communications in Computational Physics*, 28(5), 2020.
- [30] Ameya D Jagtap, Ehsan Kharazmi, and George Em Karniadakis. Conservative physics-informed neural networks on discrete domains for conservation laws: Applications to forward and inverse problems. *Computer Methods in Applied Mechanics and Engineering*, 365:113028, 2020.
- [31] Khemraj Shukla, Ameya D Jagtap, and George Em Karniadakis. Parallel physics-informed neural networks via domain decomposition. *Journal of Computational Physics*, 447:110683, 2021.
- [32] Chenhao Si and Ming Yan. Initialization-enhanced physics-informed neural network with domain decomposition (idpinn). *arXiv preprint arXiv:2406.03172*, 2024.
- [33] Chuqi Chen, Qixuan Zhou, Yahong Yang, Yang Xiang, and Tao Luo. Quantifying training difficulty and accelerating convergence in neural network-based pde solvers. *arXiv preprint arXiv:2410.06308*, 2024.
- [34] Jin Song, Ming Zhong, George Em Karniadakis, and Zhenya Yan. Two-stage initial-value iterative physics-informed neural networks for simulating solitary waves of nonlinear wave equations. *Journal of Computational Physics*, 505:112917, 2024.
- [35] Jeremy Yu, Lu Lu, Xuhui Meng, and George Em Karniadakis. Gradient-enhanced physics-informed neural networks for forward and inverse pde problems. *Computer Methods in Applied Mechanics and Engineering*, 393:114823, 2022.
- [36] Zhiyuan Zhao, Xueying Ding, and B Aditya Prakash. Pinnsformer: A transformer-based framework for physics-informed neural networks. *arXiv preprint arXiv:2307.11833*, 2023.
- [37] Jinshuai Bai, Gui-Rong Liu, Ashish Gupta, Laith Alzubaidi, Xi-Qiao Feng, and YuanTong Gu. Physics-informed radial basis network (pirbn): A local approximating neural network for solving nonlinear partial differential equations. *Computer Methods in Applied Mechanics and Engineering*, 415:116290, 2023.
- [38] Yanzhi Liu, Ruifan Wu, and Ying Jiang. Binary structured physics-informed neural networks for solving equations with rapidly changing solutions. *arXiv preprint arXiv:2401.12806*, 2024.
- [39] Biao Yuan, He Wang, Ana Heitor, and Xiaohui Chen. f-picnn: A physics-informed convolutional neural network for partial differential equations with space-time domain. *Journal of Computational Physics*, 515:113284, 2024.
- [40] Guangtao Zhang, Huiyu Yang, Fang Zhu, Yang Chen, et al. Dasa-pinns: Differentiable adversarial self-adaptive pointwise weighting scheme for physics-informed neural networks. 2023.
- [41] Zheyuan Hu, Ameya D Jagtap, George Em Karniadakis, and Kenji Kawaguchi. Augmented physics-informed neural networks (apinns): A gating network-based soft domain decomposition methodology. *Engineering Applications of Artificial Intelligence*, 126:107183, 2023.
- [42] Sokratis J Anagnostopoulos, Juan Diego Toscano, Nikolaos Stergiopoulos, and George Em Karniadakis. Residual-based attention in physics-informed neural networks. *Computer Methods in Applied Mechanics and Engineering*, 421:116805, 2024.
- [43] Xin Li, Zhihong Xia, and Hongkun Zhang. Cauchy activation function and xnet. *arXiv preprint arXiv:2409.19221*, 2024.
- [44] Xin Li, Zhihong Jeff Xia, and Xiaotao Zheng. Model comparisons: Xnet outperforms kan. *arXiv preprint arXiv:2410.02033*, 2024.



- [45] Ziya Uddin, Sai Ganga, Rishi Asthana, and Wubshet Ibrahim. Wavelets based physics informed neural networks to solve non-linear differential equations. *Scientific Reports*, 13(1):2882, 2023.
- [46] Lu Lu, Raphael Pestourie, Wenjie Yao, Zhicheng Wang, Francesc Verdugo, and Steven G Johnson. Physics-informed neural networks with hard constraints for inverse design. *SIAM Journal on Scientific Computing*, 43(6):B1105–B1132, 2021.
- [47] Natarajan Sukumar and Ankit Srivastava. Exact imposition of boundary conditions with distance functions in physics-informed deep neural networks. *Computer Methods in Applied Mechanics and Engineering*, 389:114333, 2022.
- [48] Aditi Krishnapriyan, Amir Gholami, Shandian Zhe, Robert Kirby, and Michael W Mahoney. Characterizing possible failure modes in physics-informed neural networks. *Advances in neural information processing systems*, 34:26548–26560, 2021.
- [49] Pratanu Roy and Stephen T Castonguay. Exact enforcement of temporal continuity in sequential physics-informed neural networks. *Computer Methods in Applied Mechanics and Engineering*, 430:117197, 2024.